Energy transfer in Rayleigh-Taylor instability

Andrew W. Cook and Ye Zhou
Lawrence Livermore National Laboratory, University of California, Livermore, California 94551
(Received 1 November 2001; revised manuscript received 8 February 2002; published 30 August 2002)

The spatial structure and energy budget for Rayleigh-Taylor instability are examined using results from a $512\times512\times2040$ point direct numerical simulation. The outer-scale Reynolds number of the flow follows a rough t^3 power law and reaches a final value of about 5500. Taylor microscales and Reynolds numbers are plotted to characterize anisotropy in the flow and document progress towards the mixing transition. A mixing parameter is defined which characterizes the relative rates of entrainment and mixing in the flow. The spectrum of each term in the kinetic energy equation is plotted, at regular time intervals, as a function of the inhomogeneous direction and the two-dimensional wave number for the homogeneous directions. The energy spectrum manifests the beginning of an inertial range by the latter stages of the simulation. The production and dissipation spectra become increasingly opposite and separate in wave space as the flow evolves. The transfer spectrum depends strongly on the inhomogeneous direction, with the net transfer being from large to small scales. Energy transfer at the bubble/spike fronts is strictly positive. Extensive cancellation occurs between the pressure and advection terms. The dilatation term produces negligible energy transfer, but its overall effect is to move energy from high to low density regions.

DOI: 10.1103/PhysRevE.66.026312 PACS number(s): 47.27.Ak, 47.27.Cn

I. INTRODUCTION

Rayleigh-Taylor instability (RTI) occurs at the interface between two fluids of different densities whenever the heavier fluid is decelerated by the lighter fluid [1–4]; i.e., if density and pressure gradients are in opposite directions, then vorticity, deposited at the interface through baroclinic torque, will cause the fluids to interpenetrate and mix. Richtmyer-Meshkov instability (RMI) corresponds to the case of impulsive acceleration of an interface [5,6], e.g., shock passage, and is sometimes considered a special case of RTI (with time-dependent acceleration). RTI presents a serious design challenge for inertial confinement fusion (ICF) capsules, where high density shells are decelerated by low density fuel. Depending on the acceleration history and the ratio of shell radius to thickness, RTI may lead to break up of the shell prior to ignition and/or significant mixing of the fuel with the plastic ablator [7]. RTI also plays a prominent role in supernovae, where ejecta are decelerated by circumstellar matter [8,9]. Furthermore, mixing from RTI alters thermonuclear burn in supernovae in such a manner as to affect the rates of formation of heavy elements; hence, the relative abundance of elements in the universe, and the corresponding potential for life, are directly related to astrophysical RTI mixing.

Most RTI research thus far has focused on predicting the rate of growth of the turbulent mixing zone [10–15]. Mixing zone amplitudes are routinely measured in high-energy laser experiments conducted at very high Reynolds number [16]. In its early stages, RTI growth is characterized by ''spikes'' of heavy fluid penetrating into light material and ''bubbles'' of light fluid rising into heavy material. In the strongly nonlinear stages, the bubbles and spikes merge to form larger structures. If the only imposed length scale is from a constant acceleration, then the mixing layer will grow quadratically in time; e.g., a growth constant ''α'' can be defined and measured [17,18,10–13]. However, if long wavelength perturbations (compared to domain size) are present, the scaling analysis is more complicated and growth may not be quadratic [19].

The range of scales participating in RTI dynamics continually grows as the flow evolves. Kelvin-Helmholtz instabilities, occurring along the sides of the interpenetrating fingers, along with vortex stretching and bending motions, serve to broaden the energy spectrum. Eventually the flow may become fully turbulent, while still remaining highly anisotropic. A complete description of the flow field requires resolution down to the Kolmogorov scale [20,21]. Due to limitations of diagnostics, laser experiments performed thus far have not yielded much information on the internal structure of the mixing region. Larger-scale experiments [22–24] have provided some information on mixing zone structure, but lack the resolution necessary for a close investigation of the energy budget.

Over the past three decades, direct numerical simulation (DNS) has emerged as an accepted surrogate for experiment when detailed information, not readily measured in the laboratory, is needed. DNS is restricted to low Reynolds number flows, due to the limited range of wave numbers that can be supported on a computational mesh. Nevertheless, it has proven capable of following the three phases of turbulent mixing identified by Eckart [25], i.e., entrainment, stirring, and molecular mixing. It also provides a complete, three-dimensional, time-dependent description of the flow field. DNS data of RTI flow can be used to test and/or tune models for the overall growth of the mixing region, and for developing subgrid-scale (SGS) models for large eddy simulation. The latter is intimately connected with energy transfer to and from unresolved scales. The primary goal of this paper is to gain insight into the energy transfer processes in order to guide future SGS model development.

The outline of this paper is as follows. In Sec. II, the

governing equations and solution technique of the DNS are described. In Sec. III, flow visualizations are presented, along with statistical measures of flow structure, such as growth rates and Reynolds numbers. In Sec. IV, a variable-density formulation is proposed for energy transfer analyses previously performed for isotropic [26–31], anisotropic [32], and wall-bounded [33] flows. The analysis is carried out in Sec. V, where the spectrum of each term in the kinetic energy equation is computed from the DNS data. Finally, conclusions are given in Sec. VI.

II. DIRECT NUMERICAL SIMULATION

A. Governing equations

The conservation laws governing the flow of two incompressible fluids in a gravitational field with no surface tension are

$$\frac{\partial \rho Y_l}{\partial t}+\frac{\partial \rho u_j Y_l}{\partial x_j}=\frac{\partial}{\partial x_j}\left(\rho D \frac{\partial Y_l}{\partial x_j}\right) \quad (l=1,2), \tag{1}$$

$$\frac{\partial \rho u_i}{\partial t}+\frac{\partial \rho u_i u_j}{\partial x_j}=-\frac{\partial p}{\partial x_i}+\frac{\partial \tau_{ij}}{\partial x_j}+\rho g_i, \tag{2}$$

where

$$\tau_{ij}=2\mu\left(S_{ij}-\frac{1}{3}\delta_{ij}\frac{\partial u_k}{\partial x_k}\right),$$

$$S_{ij}=\frac{1}{2}\left(\frac{\partial u_i}{\partial x_j}+\frac{\partial u_j}{\partial x_i}\right).$$

Here ρ is the mixture density, Y_l is the mass fraction of species l, u_i is the mass-averaged mixture velocity, p is the pressure, D is the Fickian diffusivity, μ is the dynamic viscosity, and $g_i=(0,0,-g)$ is the acceleration. The mass fractions satisfy

$$Y_1(\mathbf{x},t)+Y_2(\mathbf{x},t)=1 \tag{3}$$

and, defining ρ_1 and ρ_2 to be the constant densities of the light and heavy fluids, respectively, the specific volume satisfies

$$\frac{1}{\rho(\mathbf{x},t)}=\frac{Y_1(\mathbf{x},t)}{\rho_1}+\frac{Y_2(\mathbf{x},t)}{\rho_2}. \tag{4}$$

Equations (1), (3), and (4) can be used to derive the following divergence relation for miscible fluids [34]:

$$\frac{\partial u_j}{\partial x_j}=-\frac{\partial}{\partial x_j}\left(\frac{D}{\rho}\frac{\partial \rho}{\partial x_j}\right). \tag{5}$$

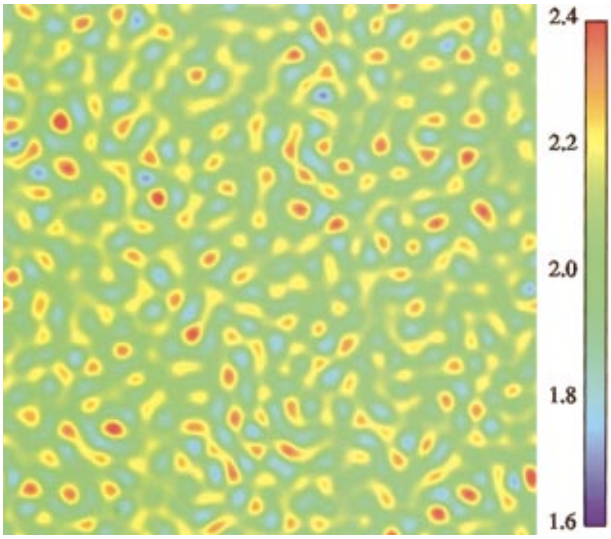

FIG. 1. (Color) Initial density perturbations on $z=0$ plane.

Hence, for incompressible mixing, a convenient equation for ρ is

$$\frac{\partial \rho}{\partial t}+u_j\frac{\partial \rho}{\partial x_j}=\rho\frac{\partial}{\partial x_j}\left(\frac{D}{\rho}\frac{\partial \rho}{\partial x_j}\right). \tag{6}$$

B. Solution technique

The equations were solved in nondimensional form, with length measured in units of box width L, time measured in units of $\sqrt{L/g}$, and density measured in units of ρ_1. The diffusivity was set to $D=\mu/\rho_1$, with the viscosity being $\mu=512^{-4/3}$ (in the units just described). The numerical scheme for solving the governing equations is described in detail in [19]. In summary, the code computes x and y derivatives spectrally via fast Fourier transform. The z derivatives are computed with an eighth-order compact scheme [35]. Periodic boundary conditions are applied in x and y, with no-slip walls imposed in z. The z grid spacing is set to $\frac{8}{13}$ times the grid spacing in x and y, in order to account for the difference in resolving power between the spectral and compact methods. Time advancement is accomplished via a pressure-projection algorithm with third-order, Adams-Bashforth-Moulton integration.

The simulation was performed on a computational mesh with $512\times512\times2040$ grid points in x, y, and z directions, respectively. The bottom $(\frac{17}{32})$ of the domain was initialized with $\rho=\rho_1=1$ and the top $(\frac{15}{32})$ portion with $\rho=\rho_2=3$. The density interface between the fluids was specified in the same manner as in [19], i.e., as an error function in z (five grid points thick) with isotropic perturbations in x and y. The perturbed interface was initially located at the $z=0$ plane. Diffusion velocities were initialized as in [19] in order to satisfy the divergence relation (5).

The spectral/compact algorithm was chosen to ensure that numerical dissipation did not enter into the calculation. No filtering or artificial diffusion of any kind was applied in the simulation, i.e., the viscous and diffusive terms in Eqs. (2)

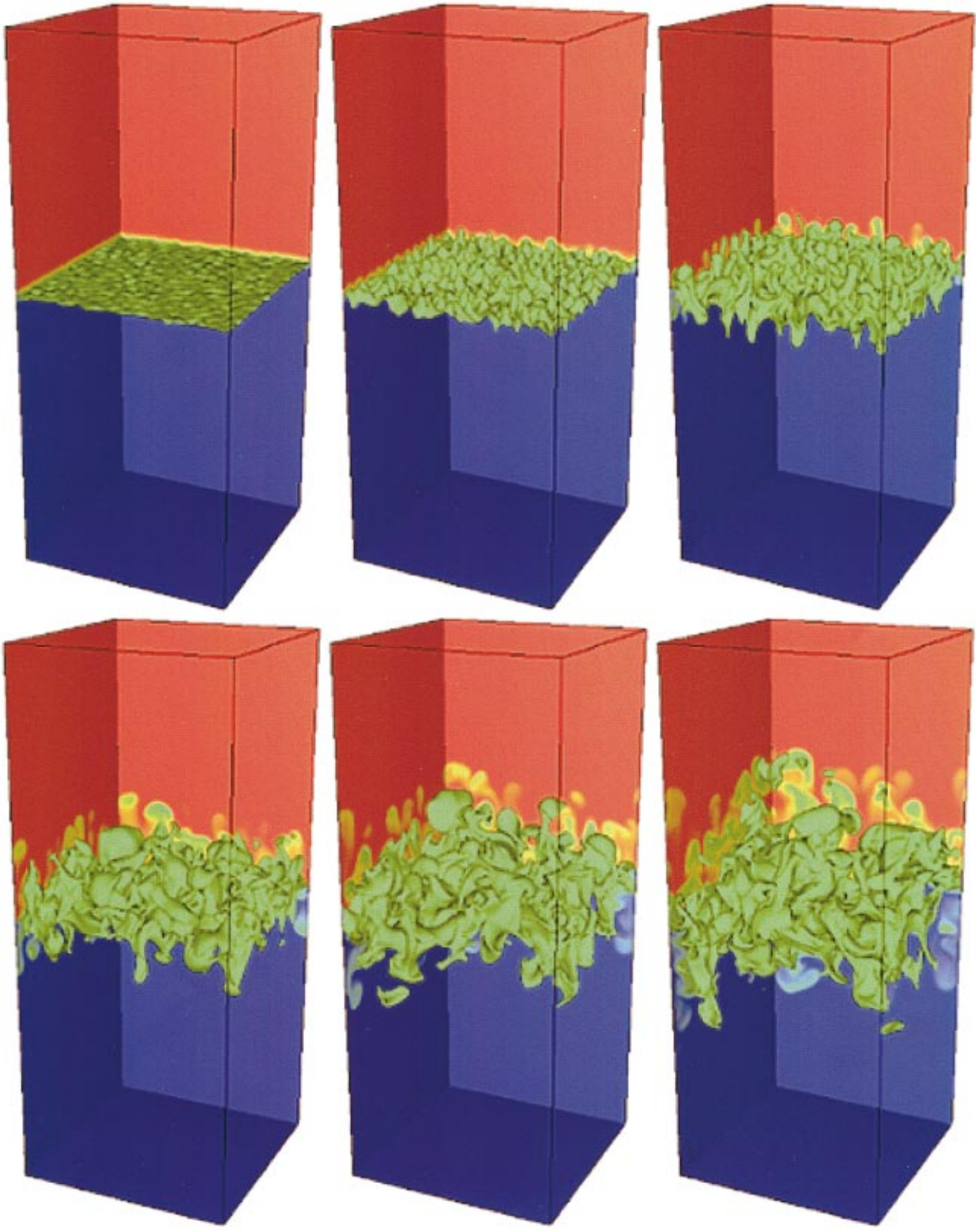

FIG. 2. (Color) Snapshots of density field from DNS of Rayleigh-Taylor instability. Images, proceeding from upper left to lower right, were taken at $t=1$, 2, 3, 4, 5, and 6. The heavy fluid is red ($\rho=3$), the light fluid is blue ($\rho=1$), and the mixed fluid is green ($\rho=2$).

and (6) were solely responsible for energy dissipation. Consequently, the simulation eventually became unstable (for Re$>$5500) once significant energy reached the Nyquist wave number. A prominent symptom of under-resolution (and consequent aliasing errors) beyond Re$=$5500 is a curling up of the energy spectrum at the highest wave numbers. The data presented herein were selected at times prior to those where significant aliasing errors occurred.

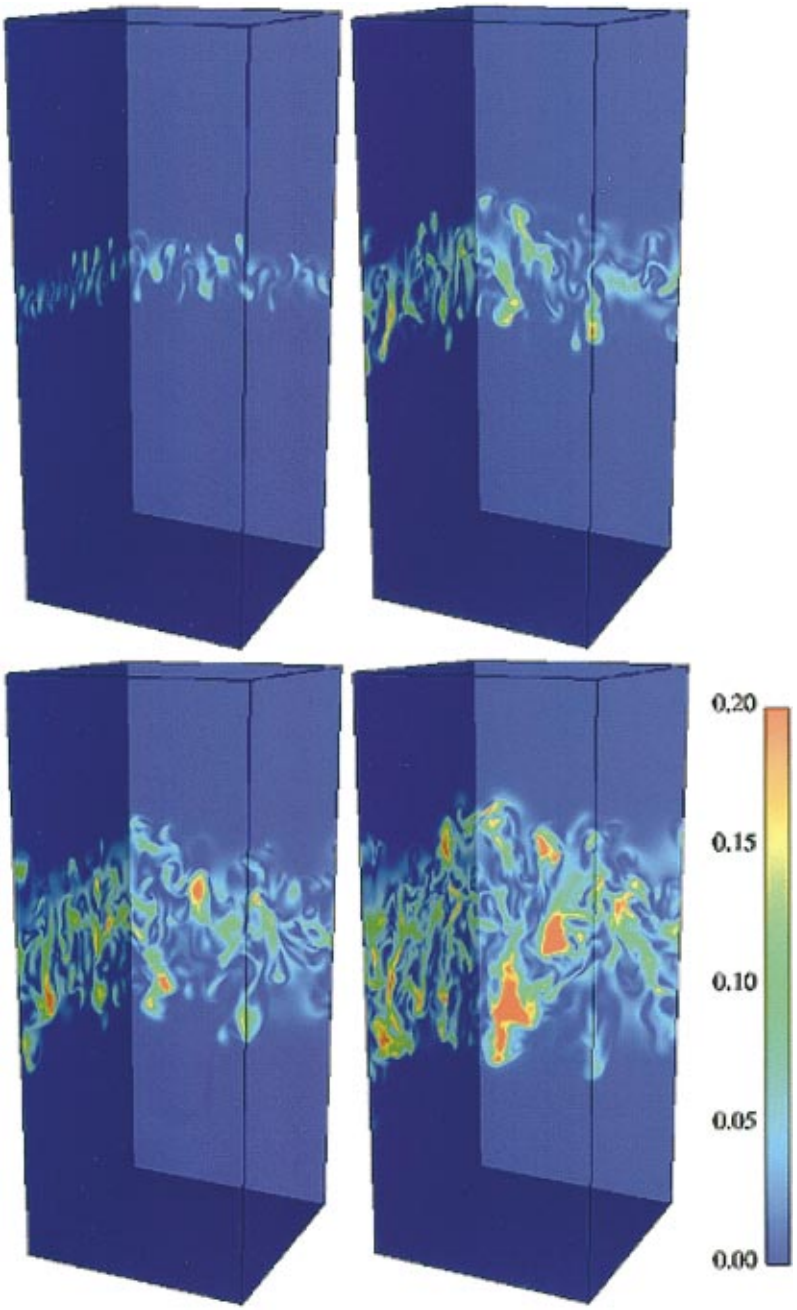

FIG. 3. (Color) Kinetic energy (κ) on side boundary planes of DNS domain. Images were taken at $t=3$, (upper left), 4 (upper right), 5 (lower left), and 6 (lower right).

III. FLOW STRUCTURE

A. Visualization

The initial perturbations are depicted in Fig. 1, which provides a top-down view of density on the $z=0$ plane at $t=0$. The flow was seeded with fine scale perturbations to minimize the influence of the periodic boundary conditions. Figure 2 displays a time sequence of the density field. The images, taken at unit time intervals, illustrate the evolution of the fluid interface (defined as the $\rho=2$ isosurface). The early evolution is weakly nonlinear and is characterized by the formation of bubbles of light fluid rising upwards and spikes of heavy fluid penetrating downward. Later on, the bubbles and spikes begin to merge and the flow becomes strongly nonlinear.

The kinetic energy, $\kappa \equiv \rho u_i u_i/2$, on the back, bottom, and side planes of the flow domain is shown in Fig. 3 for $t=3$, 4, 5, and 6. It grows rapidly and appears to be fairly evenly distributed across the mixing layer. The gravitational potential provides the source for kinetic energy production. Figure 4 displays the kinetic energy on the $z=0$ plane at the same times. Like the density field, the kinetic energy is homogeneous and isotropic in x and y. Also, large values of κ appear to become concentrated in localized regions of the flow.

The source of vorticity (and consequently energy generation) is the baroclinic torque term in the vorticity equation, which is nonzero only in the mixing region. The magnitude of vorticity, $\|\nabla \times \mathbf{u}\|$, and the magnitude of baroclinic torque, $\|\nabla \rho \times \nabla p\|/\rho$, at $t=6$, are plotted in Fig. 5. A few spikelike and bubblelike structures are discernible in the fields; how-

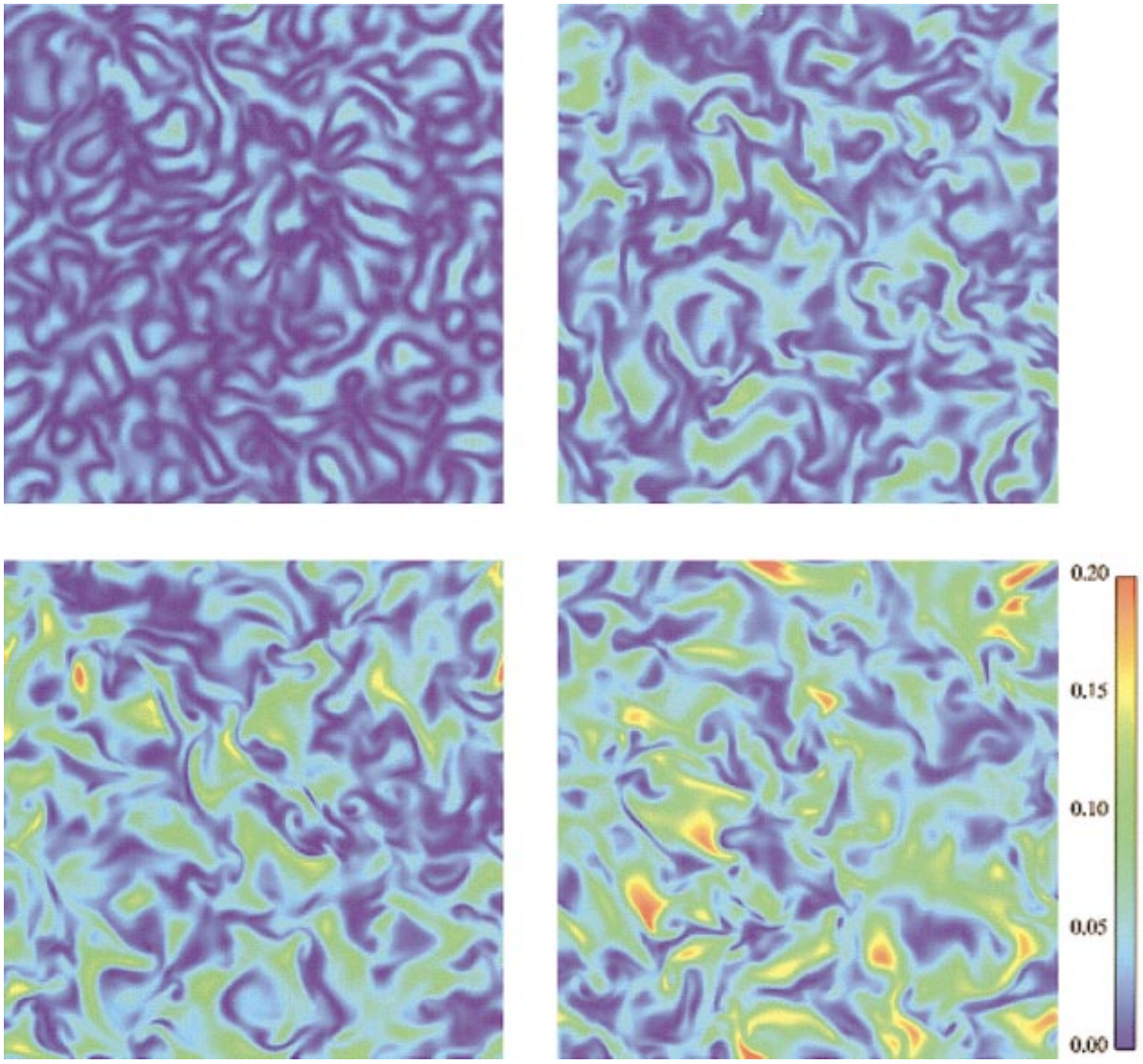

FIG. 4. (Color) Kinetic energy (κ) on $z=0$ plane at $t=3$, (upper left), 4 (upper right), 5 (lower left), and 6 (lower right).

ever, the fields are quite chaotic. Early on, when the bubbles and spikes are growing more or less independently, and hence are readily identified, vorticity (and consequently energy) is primarily generated along the sides of the structures. However, by late time, the flow has become weakly turbulent and vorticity generation occurs throughout the mixing zone. The complexity of the baroclinic torque field increases as centrifugal forces pull pressure gradients out of alignment with the gravity vector.

B. Statistics

The penetration lengths of the bubbles and spikes, $h_b(t)$ and $h_s(t)$, respectively, are defined as in [19], i.e., by averaging the heavy fluid mole fraction $[X=(\rho-\rho_1)/(\rho_2-\rho_1)]$ in x and y, and measuring the distance from $z=0$ for which $\langle X\rangle_{xy}\leqslant 0.99$ and $\langle X\rangle_{xy}\geqslant 0.01$ ($\langle\rangle_{xy}$ denoting horizontal average). The bubble and spike penetrations are plotted in Fig. 6. The change in slope around $t=2$ occurs as modal growth overtakes diffusive growth.

The outer-scale Reynolds number is plotted, versus time, in Fig. 7. The Reynolds number is based on the vertical extent of the mixing region, $h=h_b-h_s$, and its rate of growth, $\dot{h}$, i.e.,

$$\mathrm{Re}=\frac{(\rho_1+\rho_2)\dot{h}h}{2\mu}. \tag{7}$$

The Reynolds number grows roughly like t^3, which is expected if $h\sim t^2$ and $\dot{h}\sim t$. (Reasons why h may depart from quadratic growth are discussed in [19].) The terminal outer-scale Reynolds number of 5500 is about a third of the Reynolds number $[(1-2)\times 10^4]$ suggested by Dimotakis [36] as the critical value for reaching the mixing transition and achieving fully developed turbulence. It should be noted, however, that the Reynolds number for mixing transition has yet to be documented for RTI flow. If data above the mixing transition could be obtained for RTI flow, it would be inter-

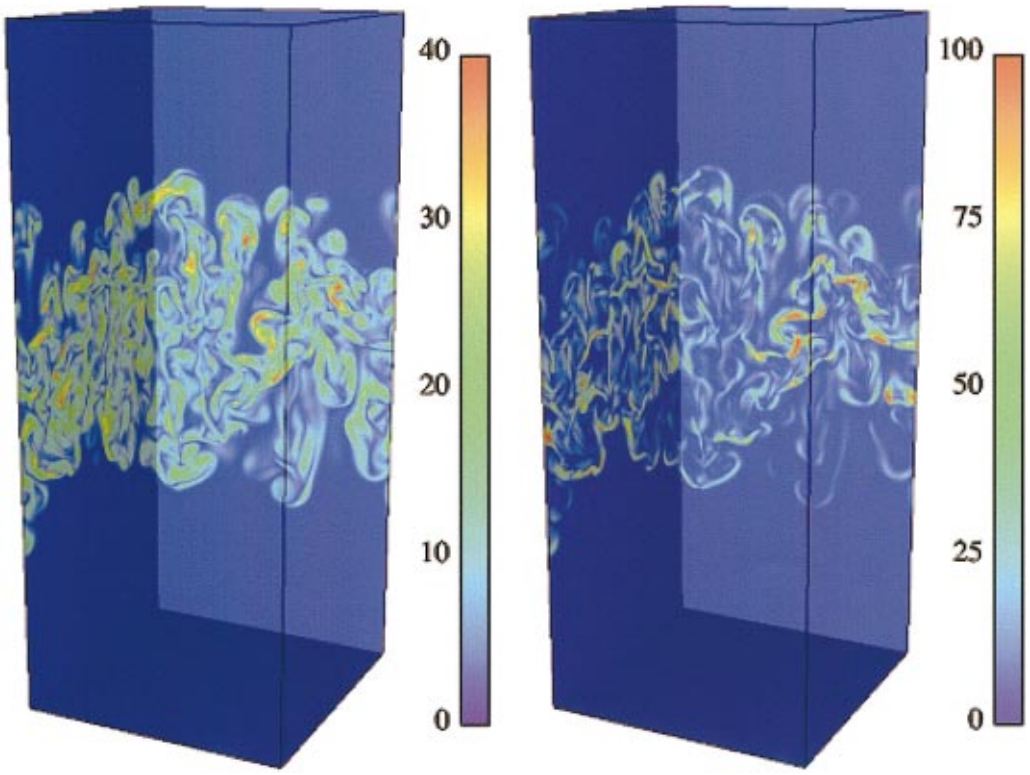

FIG. 5. (Color) Magnitude of vorticity (left) and magnitude of baroclinic torque (right) at $t=6$.

esting to see if the ''hot spots'' in kinetic energy would persist or if the energy would become more evenly distributed.

It is possible to define Taylor microscales and Reynolds numbers for this flow in a manner that accommodates the anisotropic forcing. A microscale in the i direction can be defined as [37,38]

$$\lambda_i=\left[\frac{\langle u_i^2\rangle_{xy}}{\langle(\partial u_i/\partial x_i)^2\rangle_{xy}}\right]^{1/2} \quad (\text{no sum on } i), \tag{8}$$

with statistics computed in the $(z=0)$ plane. With statistical isotropy in the $(z=0)$ plane, the x and y microscales are very close and can be averaged to define a single horizontal microscale,

$$\lambda_{xy}=\frac{\lambda_x+\lambda_y}{2}. \tag{9}$$

Figure 8 depicts the temporal growth of the vertical and horizontal Taylor microscales in the $(z=0)$ plane. The vertical and horizontal scales both grow as the bubbles increase in size, broadening the velocity correlation functions. The difference between the vertical and horizontal scales gives a

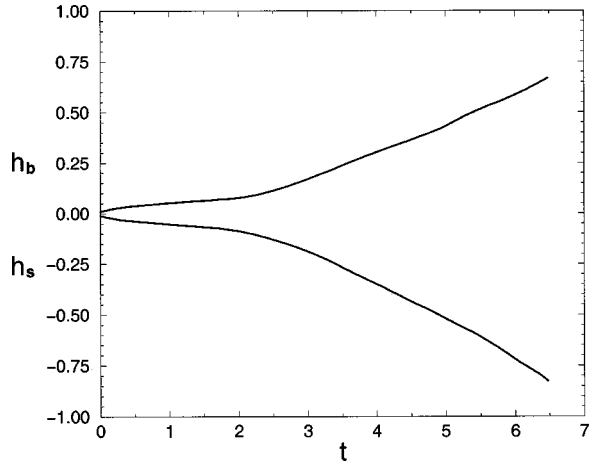

FIG. 6. Amplitude of bubbles (h_b) and spikes (h_s) in the mixing region. The total width of the layer is $h=h_b-h_s$.

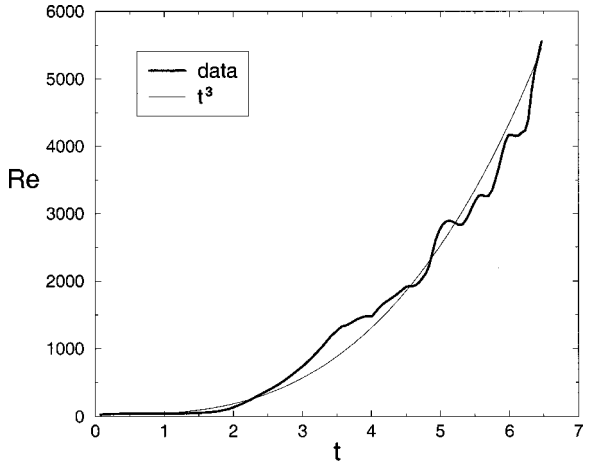

FIG. 7. Outer-scale Reynolds number, based on extent and rate of growth of mixing region.

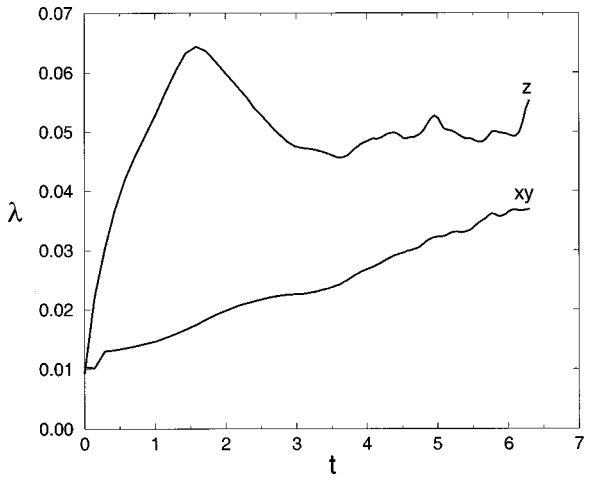

FIG. 8. Vertical (labeled *z*) and horizontal (labeled *xy*) Taylor microscales on the $z=0$ plane.

direct measure of anisotropy in the flow. The ratio λ_z/λ_{xy} starts out near unity, increases during the diffusive growth stage to a maximum value of about 3.7, and then appears to asymptote to a value around 1.4 in the far nonlinear regime.

Figure 9 depicts the temporal evolution of the horizontal and vertical Taylor Reynolds numbers on the $(z=0)$ plane. These are defined as

$$\mathrm{Re}_{\lambda,i}=\frac{\langle\rho\rangle_{xy}\lambda_i[\langle u_i^2\rangle_{xy}]^{1/2}}{\mu} \quad (\text{no sum on } i), \qquad (10)$$

again, with spatial averages computed in the $(z=0)$ plane. As with the microscales, horizontal isotropy permits a horizontal Taylor Reynolds number to be defined as the average of $\mathrm{Re}_{\lambda,x}$ and $\mathrm{Re}_{\lambda,y}$, i.e.,

$$\mathrm{Re}_{\lambda,xy}=\frac{\mathrm{Re}_{\lambda,x}+\mathrm{Re}_{\lambda,y}}{2}. \qquad (11)$$

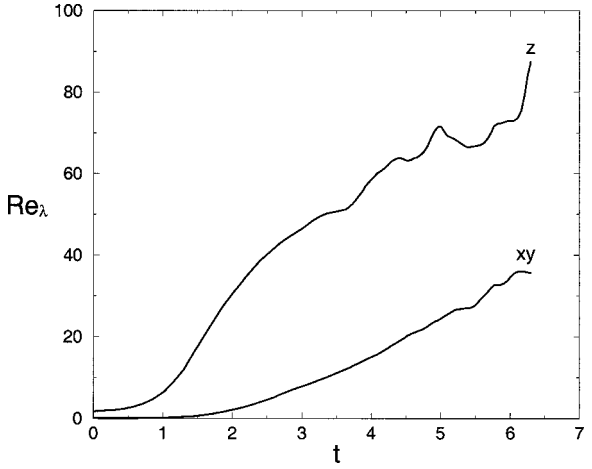

FIG. 9. Vertical (*z* label) and horizontal (*xy* label) Taylor Reynolds numbers on the $z=0$ plane.

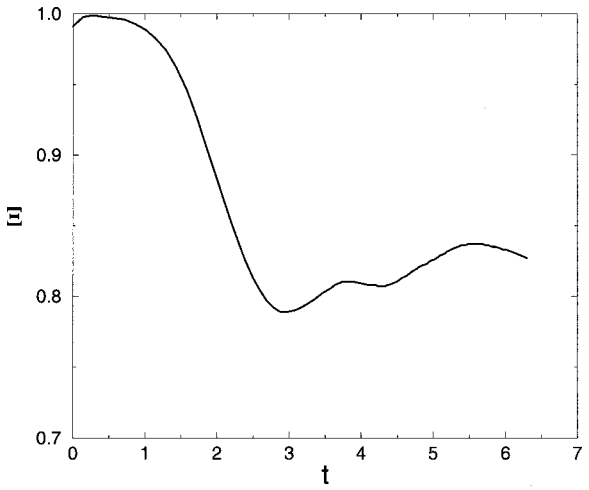

FIG. 10. Mixing parameter, indicating the ratio of actual chemical product (for a hypothetical infinite-rate reaction) to the product that would be formed if the fluid inside the mixing region were completely mixed (no *xy* variation).

The anisotropy in microscales (Fig. 8) is also manifest in the Taylor Reynolds numbers. A Taylor Reynolds number of roughly 100 is required to cross the mixing transition [36]. Judging from the proximity of the outer-scale Reynolds number to the critical value of 10 000–20 000, it appears that the transition criterion would probably apply best to the horizontal Taylor Reynolds number, rather than the vertical.

In order to quantify the degree of mixing within the layer, a parameter, analogous to the Youngs [13] ''molecular mixing fraction,'' (Θ) is defined. Assuming a passive, equilibrium chemical reaction between fluids, the chemical product is

$$X_p=\begin{cases} X/X_s & \text{if } X\leqslant X_s \\ (1-X)/(1-X_s) & \text{if } X>X_s \end{cases}, \qquad (12)$$

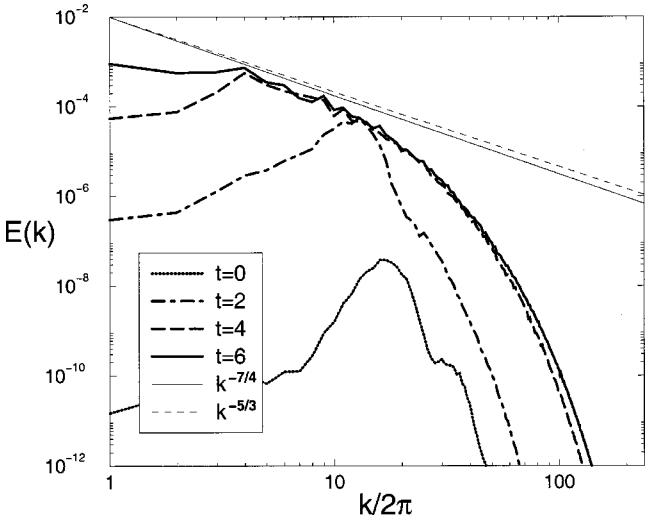

FIG. 11. Evolution of two-dimensional energy spectrum (*E*) at $z=0$.

where X_s is the (heavy-fluid) mole fraction for a stoichiometric mixture, here taken as $X=\frac{1}{2}$. A mixing parameter, Ξ, is defined as the ratio of mixed to entrained fluid, i.e.,

$$\Xi = \frac{\int_H \langle X_p(X)\rangle_{xy} dz}{\int_H X_p(\langle X\rangle_{xy}) dz}, \tag{13}$$

where H is the height of the flow domain. Thus, $\Xi=1$ indicates fluids are completely mixed within the mixing zone; whereas, $\Xi=0$ corresponds to fully segregated fluids (immiscible case). Note that with no perturbations ($X=\langle X\rangle_{xy}$), for an increasingly sharp interface, the numerator and denominator go to zero at the same rate; hence, $\Xi=1$ for a Heaviside function. The mixing parameter Ξ is plotted in Fig. 10 as a function of time. Initially, the layer is diffuse with small amplitude perturbations; hence, Ξ starts out near unity. As the perturbations grow, they entrain fluid at a rate proportional to their wavelengths (longer wavelengths result in bigger ''gulps'' of pure fluid). At early times, the rate of entrainment exceeds the rate of mixing and Ξ decreases. This is a consequence of the fact that, early on, the surface area across which the fluids can diffuse is relatively small. However, later on the interface begins to wrinkle due to baroclinic vorticity (mushroom caps) and Kelvin-Helmholtz instabilities in the shearing regions along the mushroom necks; the interfacial surface area then rapidly increases, the mixing rate overtakes the entrainment rate, and the curve reverses direction. The curve appears to asymptote to a value somewhere around 0.8; however, mixing and entrainment rates have not come into balance within the time span of the simulation. Furthermore, this curve is likely to rise after the mixing transition occurs.

IV. ENERGY BUDGET

In order to extend the methodology of constant-density energetics to the variable-density case, a new variable is introduced, i.e.,

$$v_i \equiv \rho^{1/2} u_i, \tag{14}$$

such that, the kinetic energy may be written as $\kappa = v_i v_i/2$. This variable has been used for similar purposes by various authors [39–41]. The left-hand side of the Navier-Stokes equation can then be written as

$$\begin{aligned}\frac{\partial \rho u_i}{\partial t} + \frac{\partial \rho u_i u_j}{\partial x_j} &= \rho^{1/2}\frac{\partial v_i}{\partial t} + \frac{1}{2}\rho^{-1/2} v_i \frac{\partial \rho}{\partial t} \\ &\quad + \rho^{1/2}\frac{\partial v_i u_j}{\partial x_j} + \frac{1}{2}\rho^{-1/2} v_i u_j \frac{\partial \rho}{\partial x_j} \\ &= \rho^{1/2}\left(\frac{\partial v_i}{\partial t} + \frac{\partial v_i u_j}{\partial x_j} - \frac{1}{2} v_i \frac{\partial u_k}{\partial x_k}\right),\end{aligned}$$

such that the transport equation for v_i becomes

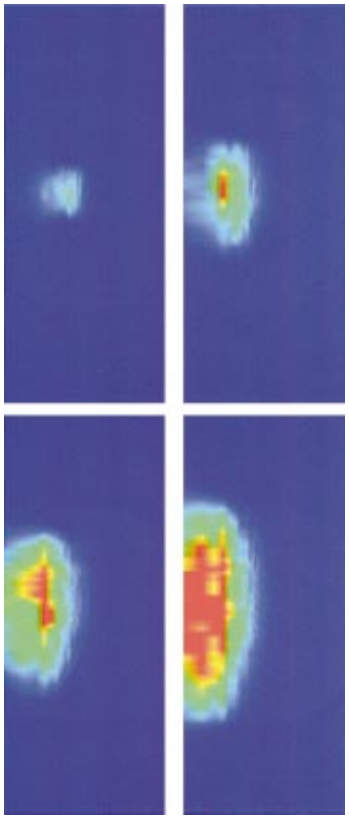

FIG. 12. (Color) Energy spectrum (E) versus z (vertical) and $\log_{10}(k)$ (horizontal) at $t=3$ (top left), 4 (top right), 5 (lower left), and 6 (lower right). Blue$=0$ and red$=5\times10^{-4}$.

$$\begin{aligned}\frac{\partial v_i}{\partial t} &= \rho^{1/2} g_i - \frac{\partial v_i u_j}{\partial x_j} - \rho^{-1/2}\frac{\partial p}{\partial x_i} + \frac{1}{2} v_i \frac{\partial u_k}{\partial x_k} \\ &\quad + 2\rho^{-1/2}\frac{\partial}{\partial x_j}\left[\mu\left(S_{ij} - \frac{1}{3}\delta_{ij}\frac{\partial u_k}{\partial x_k}\right)\right].\end{aligned} \tag{15}$$

For simplicity, Eq. (15) is rewritten as

$$\frac{\partial v_i}{\partial t} = F_i + N_i + D_i, \tag{16}$$

where the buoyant forcing is

$$F_i = \rho^{1/2} g_i, \tag{17}$$

the nonlinear (quadratic, pressure, and dilatation) contribution is

$$N_i = -\frac{\partial v_i u_j}{\partial x_j} - \rho^{-1/2}\frac{\partial p}{\partial x_i} + \frac{1}{2} v_i \frac{\partial u_k}{\partial x_k}, \tag{18}$$

and the viscous diffusion is

$$D_i = 2\rho^{-1/2}\frac{\partial}{\partial x_j}\left[\mu\left(S_{ij} - \frac{1}{3}\delta_{ij}\frac{\partial u_k}{\partial x_k}\right)\right]. \tag{19}$$

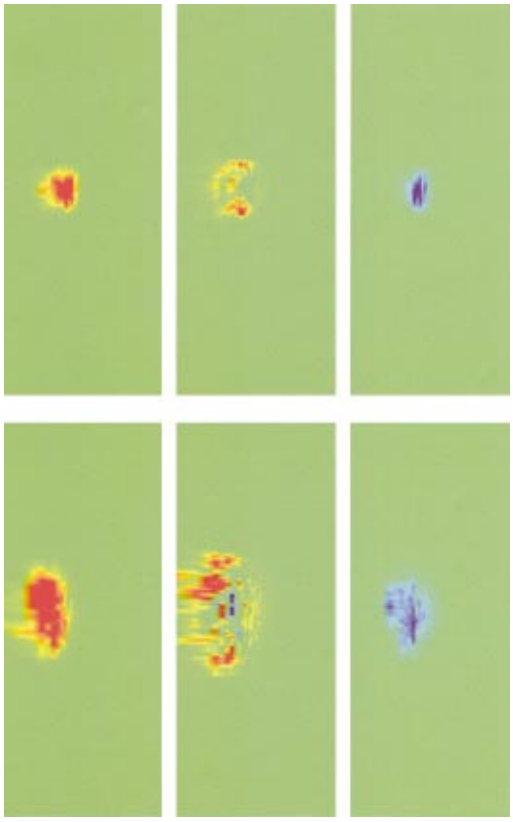

FIG. 13. (Color) Production (Π: left), transfer ($\mathcal{T}$: middle), and dissipation ($\mathcal{E}$: right) spectra versus z (vertical) and $\log_{10}(k)$ (horizontal) at $t=3$ (top) and 4 (bottom). Blue$=-2\times10^{-4}$, green$=0$, and red$=2\times10^{-4}$.

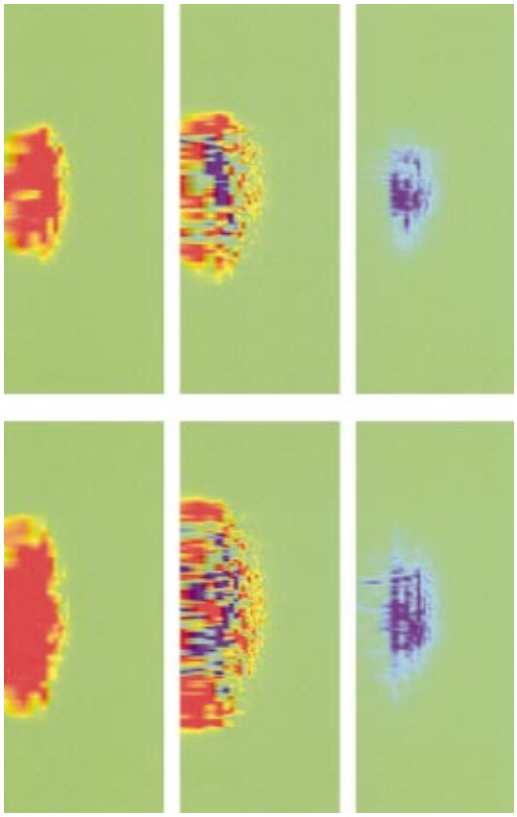

FIG. 14. (Color) Production (Π: left), transfer ($\mathcal{T}$: middle), and dissipation ($\mathcal{E}$: right) spectra versus z (vertical) and $\log_{10}(k)$ (horizontal) at $t=5$ (top) and 6 (bottom). Blue$=-2\times10^{-4}$, green$=0$, and red$=2\times10^{-4}$.

Now let $\hat{v}_i$, $\hat{F}_i$, $\hat{N}_i$, and $\hat{D}_i$ be horizontal Fourier transforms of v_i, F_i, N_i, and D_i, respectively; e.g., $\hat{v}_i(\mathbf{k},z,t)=\mathcal{F}_{xy}\{v_i(\mathbf{x},t)\}$, where $\mathbf{k}=(k_x,k_y)$ is the horizontal wave vector. If $\hat{v}_i^*(\mathbf{k},z,t)$ denotes the complex conjugate of $\hat{v}_i(\mathbf{k},z,t)$, then multiplying the transform of Eq. (16), and its conjugate, by $\hat{v}_i^*$ and $\hat{v}_i$, respectively, and adding the equations together yields

$$\frac{\partial \hat{v}_i^* \hat{v}_i}{\partial t}=\hat{v}_i^*\hat{F}_i+\hat{v}_i\hat{F}_i^*+\hat{v}_i^*\hat{N}_i+\hat{v}_i\hat{N}_i^*+\hat{v}_i^*\hat{D}_i+\hat{v}_i\hat{D}_i^*. \tag{20}$$

Integrating Eq. (20) over Fourier annuli of radius $k=\sqrt{k_x^2+k_y^2}$ leads to the energy budget equation

$$\frac{\partial}{\partial t}E(k,z,t)=\Pi(k,z,t)+\mathcal{T}(k,z,t)+\mathcal{E}(k,z,t), \tag{21}$$

where the kinetic energy is

$$E=\frac{1}{2}\oint(\hat{v}_i^*\hat{v}_i)d\sigma, \tag{22}$$

the production from gravity is

$$\Pi=\frac{1}{2}\oint(\hat{v}_i^*\hat{F}_i+\hat{v}_i\hat{F}_i^*)d\sigma, \tag{23}$$

the nonlinear transfer is

$$\mathcal{T}=\frac{1}{2}\oint(\hat{v}_i^*\hat{N}_i+\hat{v}_i\hat{N}_i^*)d\sigma, \tag{24}$$

and the viscous dissipation is

$$\mathcal{E}=\frac{1}{2}\oint(\hat{v}_i^*\hat{D}_i+\hat{v}_i\hat{D}_i^*)d\sigma, \tag{25}$$

with $d\sigma$ being a differential element of a wave space annulus.

There are three contributions to the nonlinear energy transfer. The first is from the quadratic term, which is responsible for passive-vector advection, while the second and third contributions are from pressure and dilatation effects. In order to ascertain the relative importance of each process, the total nonlinear transfer is subdivided into each individual component, i.e.,

$$\mathcal{T}(k,z,t)=\mathcal{T}_q(k,z,t)+\mathcal{T}_p(k,z,t)+\mathcal{T}_d(k,z,t), \tag{26}$$

where

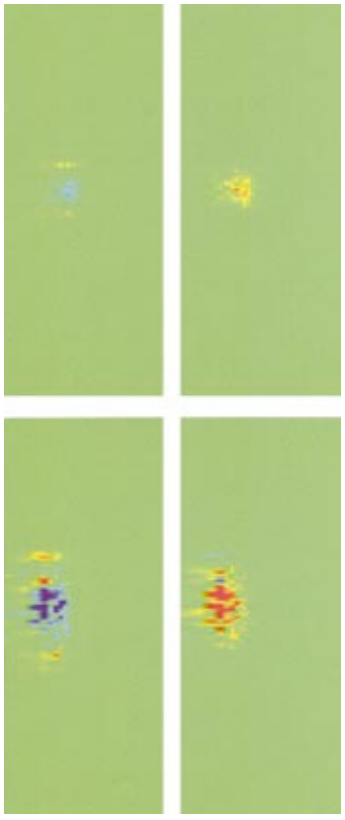

FIG. 15. (Color) Quadratic ($\mathcal{T}_q$: left) and pressure ($\mathcal{T}_p$: right) contributions to transfer spectrum versus z (vertical) and $\log_{10}(k)$ (horizontal) at $t=3$ (top) and 4 (bottom). Blue$=-5\times10^{-4}$, green$=0$, and red$=5\times10^{-4}$.

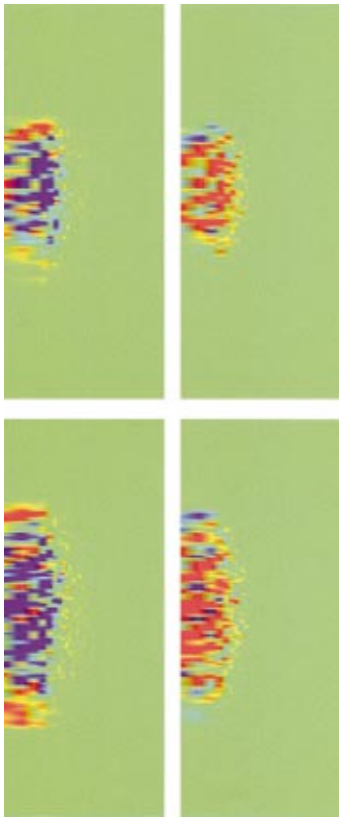

FIG. 16. (Color) Quadratic ($\mathcal{T}_q$: left) and pressure ($\mathcal{T}_p$: right) contributions to transfer spectrum versus z (vertical) and $\log_{10}(k)$ (horizontal) at $t=5$ (top), and 6 (bottom). Blue$=-5\times10^{-4}$, green$=0$, and red$=5\times10^{-4}$.

$$\mathcal{T}_m=\frac{1}{2}\oint(\hat{v}_i^*\hat{N}_{m,i}+\hat{v}_i\hat{N}_{m,i}^*)d\sigma \quad (m=q,p,d) \tag{27}$$

and

$$N_{q,i}=-\frac{\partial v_i u_j}{\partial x_j}, \tag{28}$$

$$N_{p,i}=-\rho^{-1/2}\frac{\partial p}{\partial x_i}, \tag{29}$$

$$N_{d,i}=\frac{1}{2}v_i\frac{\partial u_k}{\partial x_k}. \tag{30}$$

V. SPECTRA

The time evolution of the two-dimensional energy spectrum, $E(k,z=0,t=0,2,4,6)$, is plotted in Fig. 11. The initial diffusion velocities result in a nonzero spectrum at $t=0$. The spectrum increases by several orders of magnitude as kinetic energy is deposited into the flow. The peak of the spectrum migrates toward lower wave numbers as bubbles and spikes merge to form larger structures. The spectrum also fills out at higher wave numbers as vortex stretching and bending motions transfer energy to smaller scales. Near the end of the simulation it appears that an inertial range is just beginning to form. In [42], Zhou argues that the inertial range for the RTI flow will follow a $-\frac{7}{4}$ power law. He reasons that the spectrum will be modified from the classical Kolmogorov $(-\frac{5}{3})$ power law for isotropic turbulence as a result of the external time scale introduced by gravity. Both power laws are shown on the figure for comparison to the data. The late-time spectra appear somewhat consistent with Zhou's theory; however, the statistical fluctuations in the spectra (there are not many points in the Fourier annuli at lower wavenumbers) are larger than the difference in slope between $k^{-7/4}$ and $k^{-5/3}$. Furthermore, there is no clear beginning to the dissipation range, which appears to extend well into the lower wave numbers, thereby steepening the slope of the spectrum. Due to the closeness of the power laws, much higher Reynolds number data and improved statistics will be needed in order to discriminate between the two.

The z dependence of the energy spectrum is graphically portrayed in Fig. 12 at four different times. The plots are in a semi-Fourier domain with $\log_{10}(k)$ along the abscissa and z along the ordinate. The bulk of the energy is initially deposited at a moderate wave number, corresponding to the dominant wavelength of the density perturbations. As time progresses, $E(k,z,t)$ expands in both k and z but maintains its maximum value close to $z=0$. The spectrum decreases near the edges of the mixing zone, becoming negligible outside it.

The production (Π), transfer ($\mathcal{T}$), and dissipation ($\mathcal{E}$) spec-

tra are plotted in Figs. 13 and 14 on the same z versus $\log_{10}(k)$ domain for the same times. Early on, the peaks of the production and dissipation spectra are close to one another, but later the production moves toward lower wave numbers while the peak of the dissipation spectrum stays roughly fixed. By the end of the simulation, there is some k separation between the two, i.e., as structures merge within the mixing layer, energy is deposited at larger scales. The increasing separation of peaks between the production and dissipation spectra is a direct result of the increasing Reynolds number for this transitional flow. As time progresses, both spectra advance in z and k, becoming increasingly large and opposite.

In contrast to the straightforward nature of Π and $\mathcal{E}$, the transfer spectrum behaves in a very complicated manner. It exhibits an intricate web of positive and negative regions, interspersed over a wide range in z and k. At higher wave numbers $\mathcal{T}$ is mostly positive, indicating a net cascade of energy to smaller scales. It is also positive at the top and bottom of the mixing zone, suggesting production of energy at the bubble and spike fronts. Inside the mixing zone, backscatter appears approximately equal to forwardscatter. It further appears that, at each instant in time, some z locations may be undergoing forward energy cascade, while neighboring regions are simultaneously experiencing inverse cascade.

In order to unravel the irregular patchwork that constitutes $\mathcal{T}$, each individual component ($\mathcal{T}_q$, $\mathcal{T}_p$, and $\mathcal{T}_d$) is plotted separately. In Figs. 15 and 16, $\mathcal{T}_q$ and $\mathcal{T}_p$ are plotted on the same semi-Fourier domain and at the same times as before. The dilatation spectrum, $\mathcal{T}_d$, is plotted (at all four times) in Fig. 17. The dilatation spectrum is roughly two orders of magnitude smaller than $\mathcal{T}_q$ and $\mathcal{T}_p$, and hence, makes negligible contribution to $\mathcal{T}$. Interestingly, the quadratic ($\mathcal{T}_q$) and pressure ($\mathcal{T}_p$) components are near opposites of one another, their net contribution to $\mathcal{T}$ being the result of extensive cancellation between the two. The quadratic term is mostly negative at lower wave numbers inside the mixing zone and mostly positive at higher wave numbers and near the edges of the mixing envelope. Regarding the pressure term, nearly the opposite is true, except at higher wave numbers where positive and negative regions appear to be roughly equally distributed. The net positive transfer of energy to the higher wave numbers (usual cascade picture) and to the bubble/spike fronts is thus a result of quadratic interactions; with pressure counterbalancing advection, for the most part.

As regards the dilatation, $\mathcal{T}_d$, although its influence on the energetics is likely negligible, it is interesting to observe that it is strongly polarized, i.e., positive for $z<0$ (spike region) and negative for $z>0$ (bubble region). The velocity divergence is related to diffusion through Eq. (5). The net effect of diffusion is to increase the density of fluid in the lower region and decrease the density of fluid in the upper region. This results in a net transfer of energy in the $-z$ direction due to diffusion of heavy fluid into light fluid. At late times, vigorous stirring at the center of the mixing zone causes the positive and negative regions of $\mathcal{T}_d$ to overlap.

VI. CONCLUSIONS

We have examined the flow structure and energy budget for Rayleigh-Taylor instability using the results of a high-resolution direct numerical simulation. The outer-scale Reynolds number was observed to follow a t^3 power law and reached a final value of 5500, the highest Reynolds number attained in a DNS or RTI flow to date. The curvature of velocity correlation functions, as manifest in the Taylor microscales, exhibits strong anisotropy between the vertical and horizontal directions, with a similar anisotropy observed in the Taylor Reynolds numbers. This is due to the directed forcing term in the governing equations. The energy spectrum, computed at the center of the mixing zone, appears to manifest the beginning of an inertial range by the latter stages of the simulation. Unfortunately, statistical fluctuations in the spectrum make it difficult to establish whether the inertial range follows a $-\frac{5}{3}$ Kolmogorov power law or the $-\frac{7}{4}$ power law proposed by Zhou [42].

A formulation of the kinetic energy equation was proposed, which enables straightforward extension of methodologies commonly employed for constant-density, isotropic turbulence. The spectrum of each term in the energy equation was computed as a function of height, horizontal wave number, and time. The peak of the energy spectrum migrates to lower wave numbers as structures merge inside the mixing layer. The production spectrum also moves to lower wave numbers as gravity acts on the larger structures. The dissipation spectrum expands in both z and k while its peak stays roughly fixed in wave number space. The limited Reynolds number of the DNS appears to inhibit movement of the peak

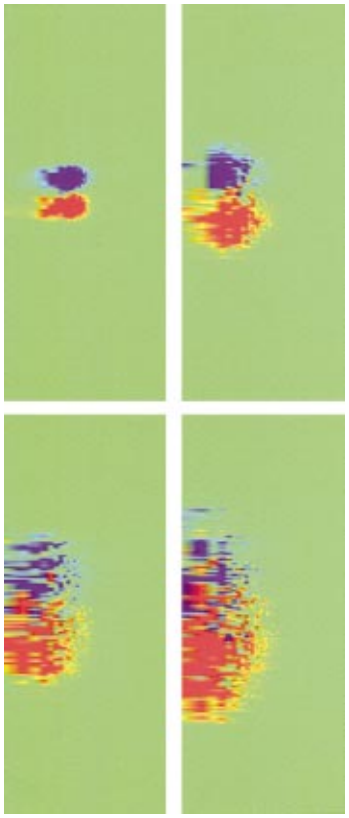

FIG. 17. (Color) Dilatation ($\mathcal{T}_d$) component of transfer spectrum versus z (vertical) and $\log_{10}(k)$ (horizontal) at $t=3$ (top left), 4 (top right), 5 (lower left), and 6 (lower right). Blue$=-7\times10^{-6}$, green $=0$, and red$=7\times10^{-6}$.

dissipation to higher wave numbers.

The transfer spectrum depends strongly on the inhomogeneous direction *z*. While the net energy transfer is from large to small scales, there is significant inverse cascade over a wide range of *z*. Energy transfer at the bubble/spike fronts is strictly positive. Examination of the individual contributions to the transfer reveals this to be due to the quadratic (advection) term. Pressure acts to counterbalance advection, such that the net transfer is substantially smaller than the transfer from either single component. The dilatation term accounts for energy transfer via diffusion of unequal-density fluids. It is very small but serves to move energy from high to low density regions.

The flow induced by Rayleigh-Taylor instability, as seen here, has rather different character than that of homogeneous, isotropic turbulence. The flow is highly anisotropic, even at small scales, as evidenced by the Taylor microscales and Reynolds numbers. Initial rates of entrainment and mixing are determined by the initial conditions. Production rates always exceed dissipation rates; hence, the kinetic energy grows rapidly in time. Furthermore, the evolution of the spectra depends sensitively on initial conditions; since the interfacial perturbations set the scale at which energy is initially injected into the flow. This has serious consequences for large eddy simulations, where the initial perturbations may be much smaller than the grid scale. In such cases, subgrid-scale models must be capable of treating not only backscatter, but also growth of spectra below the grid scale and migration of the energy peak through the cutoff wave number. The detailed analysis of the spectra, performed herein, serves as a step toward developing subgrid-scale models capable of treating RTI flows in ICF and astrophysics applications.

ACKNOWLEDGMENTS

This work was performed under the auspices of the U.S. Department of Energy by the University of California, Lawrence Livermore National Laboratory, under Contract No. W-7405-Eng-48. Additionally, we wish to thank Professor P. E. Dimotakis for many stimulating discussions on this topic and for providing keen insights into this flow.

[1] Lord Rayleigh, Scientific papers (Cambridge University Press, Cambridge, England, 1900), Vol. II, p. 200.
[2] G. I. Taylor, Proc. R. Soc. London, Ser. A **201**, 192 (1950).
[3] S. Chandrasekhar, *Hydrodynamic and Hydromagnetic Stability* (Oxford University Press, Oxford, 1961).
[4] D. Sharp, Physica D **12**, 3 (1984).
[5] R. D. Richtmyer, Commun. Pure Appl. Math. **13**, 297 (1960).
[6] E. E. Meshkov, Sov. Fluid Dyn. **4**, 101 (1969).
[7] J. Lindl, *Internal Confinement Fusion: The Quest for Ignition and Energy Gain* (Springer, New York, 1997).
[8] L. Smarr, J. R. Wilson, R. P. Barton, and R. L. Bowers, Astrophys. J. **246**, 515 (1981).
[9] W. D. Arnett, J. N. Bahcall, R. T. Kirshner, and S. E. Woosley, Annu. Rev. Astron. Astrophys. **27**, 629 (1989).
[10] K. I. Reed, Physica D **12**, 45 (1984).
[11] D. L. Youngs, Physica D **12**, 32 (1984).
[12] D. L. Youngs, Physica D **37**, 270 (1989).
[13] D. L. Youngs, Laser Part. Beams **12**, 725 (1994).
[14] G. Dimonte, Phys. Plasmas **7**, 2255 (2000).
[15] G. Dimonte and M. Schneider, Phys. Fluids **12**, 304 (2000).
[16] B. A. Remington, R. P. Drake, H. Takabe, and D. Arbett, Phys. Plasmas **7**, 1641 (2000).
[17] V. A. Andronov, S. M. Bakhrakh, E. E. Meshkov, V. N. Mokhov, V. V. Nikiforov, A. V. Pevnitskii, and A. I. Tolshmyakov, Sov. Phys. Dokl. **27**, 5 (1982).
[18] N. N. Annuchina, Yu. A. Kucherenko, V. E. Neuvazhaev, V. N. Ogibina, L. I. Shibarshov, and V. G. Yakovlev, Izv. Akad. Nauk SSSR, Mekh. Zhidk. Gaza **6**, 157 (1978).
[19] A. W. Cook and P. E. Dimotakis, J. Fluid Mech. **443**, 69 (2001).
[20] G. K. Batchelor, *The Theory of Homogeneous Turbulence* (Cambridge University Press, Cambridge, UK, 1953).
[21] A. S. Monin and A. M. Yaglom, *Statistical Fluid Mechanics* (MIT Press, Cambridge, 1975), Vol. 2.
[22] P. F. Linden and J. M. Redondo, Phys. Fluids A **3**, 1269 (1991).
[23] P. F. Linden, J. Redondo, and D. L. Youngs, J. Fluid Mech. **265**, 97 (1994).
[24] S. B. Dalziel, P. F. Linden, and D. L. Youngs, J. Fluid Mech. **399**, 1 (1999).
[25] C. Eckart, J. Mar. Res. **VII**, 265 (1948).
[26] Y. Zhou and C. G. Speziale, Appl. Mech. Rev. **51**, 267 (1998).
[27] J. A. Domaradzki and R. S. Rogallo, Phys. Fluids A **2**, 413 (1990).
[28] P. K. Yeung and J. G. Brasseur, Phys. Fluids A **3**, 884 (1991).
[29] K. Ohkitani and S. Kida, Phys. Fluids A **4**, 794 (1992).
[30] Y. Zhou, Phys. Fluids A **5**, 1092 (1993).
[31] Y. Zhou, Phys. Fluids A **5**, 2511 (1993).
[32] Y. Zhou, P. K. Yeung, and J. G. Brasseur, Phys. Rev. E **53**, 1261 (1996).
[33] J. A. Domaradzki, W. Liu, C. Hartel, and L. Kleiser, Phys. Fluids **6**, 1583 (1994).
[34] D. D. Joseph, Eur. J. Mech. B/Fluids **9**, 565 (1990).
[35] S. K. Lele, J. Comput. Phys. **103**, 16 (1992).
[36] P. E. Dimotakis, J. Fluid Mech. **409**, 69 (2000).
[37] H. Tennekes and J. L. Lumley, *A First Course in Turbulence* (MIT Press, Cambridge, 1972).
[38] K. K. Nomura and S. E. Elghobashi, Theor. Comput. Fluid Dyn. **5**, 153 (1993).
[39] C.-S. Yih, J. Fluid Mech. **9**, 68 (1960).
[40] J. L. Rodriguez Azara and G. Emanuel, Phys. Fluids **31**, 1058 (1998).
[41] S. Kida and S. A. Orszag, J. Sci. Comput. **5**, 85 (1990).
[42] Y. Zhou, Phys. Fluids **13**, 538 (2001).